IOP PUBLISHING PLASMA PHYSICS AND CONTROLLED FUSION

Plasma Phys. Control. Fusion **49** (2007) B211–B221 doi:10.1088/0741-3335/49/12B/S19

Observation of electron transport dynamics in high intensity laser interactions using multi-energy monochromatic x-ray imaging

L A Gizzi[1,2], A Giulietti[1,2,3], D Giulietti[1,2], P Köster[1,2], L Labate[1,2], T Levato[1,2], F Zamponi[4], A Lübcke[4], T Kämpfer[4], I Uschmann[4], E Förster[4], A Antonicci[5] and D Batani[5]

[1] Intense Laser Irradiation Laboratory—IPCF, Consiglio Nazionale delle Ricerche, Via Moruzzi 1, 56124 Pisa, Italy
[2] INFN, Sezione di Pisa, Largo B. Pontecorro 3, 56127 Pisa, Italy
[3] Dip. Fisica, Università di Pisa, Largo B. Pontecorro 3, 56127 Pisa, Italy
[4] Institute of Optics and Quantum Electronics, Friedrich-Schiller University, Max-Wien-Platz 1, 07743 Jena, Germany
[5] Dipartimento di Fisica G Occhialini, Università Milano Bicocca, Milano, Italy

E-mail: la.gizzi@ipcf.cnr.it

Received 6 July 2007
Published 15 November 2007
Online at stacks.iop.org/PPCF/49/B211

Abstract

We describe recent measurements in which a novel imaging technique was used to investigate the transport of high energy electrons produced by the interaction of a femtosecond laser pulse with a three-layer target at an intensity of 5×10^{19} W cm^{-2}. The imaging system was configured to work in a single-photon detection regime to identify the energy of the x-ray photons and to discriminate among Kα photons generated in each target layer. Electrons emerging from the rear side after propagation through all the target layers were also detected using a custom developed detector. The results on fast electron propagation are combined with the information obtained from electron diagnostics and are modelled using analytical and numerical codes to obtain a detailed description of electron propagation dynamics.

(Some figures in this article are in colour only in the electronic version)

1. Introduction

An efficient production of energetic electrons driven by ultraintense laser pulses is regarded as a possible way to achieve inertial fusion in the so-called fast ignitor (FI) approach [1]. In this case, high current, fast electrons beams are required to propagate and deposit energy efficiently in near solid density collisional plasmas with a consequent onset of transient magnetic fields and neutralizing plasma return current. A major effort is ongoing at large and smaller scale intense laser laboratories to develop novel and effective experimental techniques applicable to fast-ignition relevant experiments and planned future full scale installations like the European High

Power Laser Energy Research facility (HiPER) [2]. Presently, the basic mechanisms behind this complex process are mainly being investigated in laser–foil target interaction experiments. In such experiments, fast electrons generated by the laser interaction at the target interface, with energies ranging from some tens of keV up to MeV, can penetrate the underlying cold target material, leading to x-ray fluorescence emission, via inner shell ionization of the target atoms. As a consequence, Kα emission can be considered as a fundamental diagnostics for these electrons [3–6]. Also, the bremsstrahlung emission, occurring in the x-ray range, from the fast electrons has an important role, from both a theoretical and an experimental viewpoint [7, 8].

Bent Bragg crystals coupled either to x-ray films or to CCD detectors are among the most used x-ray diagnostics for laser-produced plasma x-ray emission. While allowing spatial resolution to be achieved, bent crystals in the Bragg configuration suffer from some important limitations due to the limited range of available Bragg angles. For instance, a small spectral shift of the observed Kα line due to ionization can result in a reduction of the collection efficiency [9]. Also, their use in relativistic laser–plasma interaction environments is made difficult by noise issues [10], especially in those configurations requiring short distances between source, crystal and detector.

The use of CCD detectors in the so-called single-photon regime for ultrashort and ultraintense laser–plasma x-ray spectroscopy [11, 12] is now being considered in particular in sub-PW or PW laser interaction regimes [13]. As is well known, CCD detectors, while still limited in spatial resolution when compared with x-ray films, offer a number of advantages such as high linearity, dynamic range and quantum efficiency, as well as, in some respects, a higher ease-of-use [14, 15]. When used in the single-photon regime, a CCD detector enables the spectrum of the impinging x-ray radiation to be obtained without any additional dispersing device. This is basically due to the fact that each x-ray photon absorbed in the sensitive layer of the CCD gives rise to a signal (charge) proportional to the photon energy. Due to the large number of pixels in a conventional CCD chip, a few laser shots (ideally one) are required to get an x-ray spectrum in a large energy interval, with a typical resolution well below 10% in the energy range from 1 keV to a few tens of keV.

In this paper we report on the use of a novel x-ray imaging technique for the investigation of fast electron transport in solids irradiated at relativistic intensities. The technique is based upon the use of a pin-hole camera equipped with a CCD detector working in single-photon detection. As we will see, this technique [16] allows x-ray images to be obtained which are resolved in energy over a large photon energy range. After a brief description of the experimental setup in section 3, we discuss the main aspects of the technique showing the preliminary results applied to the study of x-ray fluorescence emission due to fast electron propagation in multilayer targets.

2. The single-photon detection technique

As anticipated above in section 1, in principle, a CCD detector enables the x-ray spectrum of a given source to be retrieved without any external energy dispersing device, provided that an average of no more than one photon hits each pixel. In practice, due to the charge spreading around neighbouring pixels, this number must be typically much less than one [17]. This condition can be achieved either by increasing the source to detector distance or by placing appropriate filters to attenuate the incident flux on the CCD to the required level.

Figure 1 shows an example of a typical raw data image from a CCD detector working in a low flux regime showing individual x-ray photons. The image consists of a collection of spots (each with its own shape and signal amplitude) corresponding to a single-photon interaction with the CCD detector. Images like this are processed and the charge corresponding to each

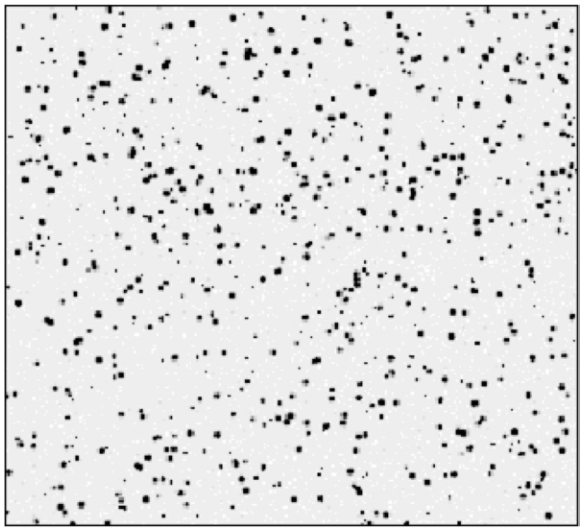

Figure 1. Typical raw data showing the low flux image obtained from detection of individual x-ray photons by a CCD detector. The image shows a 512 × 512 pixel region of the CCD. Each x-ray photon generates a charge that is proportional to its energy.

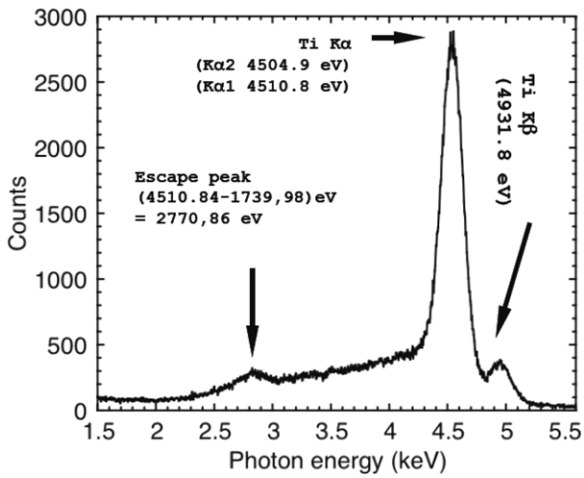

Figure 2. Spectrum of x-ray emission from a 12 μm thick Ti foil irradiated at an intensity of 5×10^{17} W cm^{-2}. The spectrum was obtained from accumulation of 30 laser shots (see text for details of the irradiation conditions).

photon event is measured and converted into incident photon energy through a calibration curve previously obtained using a set of known x-ray photon energies from both radioactive reference sources and well-characterized laser-driven sources [18]. In order to obtain a full spectrum using this technique, a number of frames like the one shown in figure 1 are required to reduce the statistical noise. This is typically obtained via integration over several laser shots. More recently, due to the increasing area and number of pixels available in commercial CCDs, single shot measurements are becoming possible. The plot in figure 2 shows an x-ray spectrum obtained from laser irradiation of a 12 μm thick Ti foil irradiated at an intensity of 5×10^{17} W cm^{-2} using the ILIL femtosecond Ti : Sa laser system which delivers up to 150 mJ

in a 65 fs duration pulse. In this case the angle of incidence was 55° and the CCD detector was facing the target from the front side, on the horizontal plane, at 10° from the target normal axis.

Clearly visible in the spectrum are the Kα and the Kβ components of x-ray emission generated by fast electron propagation in the substrate of the Ti foil target. Also visible in the spectrum is a small feature at 2.7 keV due to a small number of Ti Kα photon events in which a Kα photon from an excited atom of the Si substrate escapes from the detector sensitive area.

Recalling the image of figure 1, we observe that since this detection technique is based upon a position sensitive device (CCD) it also provides information on the landing position of each x-ray photon. Therefore, depending on the specific experimental setup, this information can be used to recover the angular distribution of incident x-ray photons or the spatial distribution at the source position. In the following section, we describe the use of a simple imaging device like a pin-hole camera coupled with the CCD detector to obtain full spectral and spatial information on the x-ray source. A detailed account of the instrumental aspects of the technique are given elsewhere [16]. Here we give an overview of the experimental setup used to test this technique in a fast electron transport experiment and we make a preliminary discussion of the x-ray emission mechanisms and how they are related to fast electrons.

3. The experimental setup

The 8 TW Ti : Sa laser system at IOQ-Jena has been used to irradiate thin foil targets at relativistic intensities. The laser provides 70 fs duration pulses with 600 mJ energy at a 10 Hz repetition rate. A 45°, $f/1.2$ off-axis parabola has been used to focus the laser beam onto the target surface down to a 5 μm^2 spot, thus reaching an intensity of about 5×10^{19} W cm^{-2} (normalized vector potential $a_0 = eA_L/m_e c^2 \simeq 4.8$). The angle of incidence on the target was about 10°. The target was moved horizontally or vertically to ensure a fresh surface to be irradiated at each shot. The targets consisted of a simple Ti foil or of a sandwich of layers of different Z materials designed to study the fast electron propagation inside the target by detecting the Kα emission from each layer.

Two pin-hole cameras were used to image out the x-ray emission from both the front and the rear side of the target. The viewing angle was about 45° with respect to the surface. Each pin-hole camera was equipped with a 5 μm diameter pin-hole, bored in a 25 μm thick Pt substrate and a back-illuminated, deep depletion CCD camera. The 1024 × 256 pixel CCD chip (Andor DX420) was typically cooled at −65 °C.

The two pin-holes were placed at about 30 mm from the target irradiation point, on both the front and rear side, and were protected from debris by using a 5 μm thick *mylar* foil. In order to obtain the required magnification, $M \simeq 10$, the two CCD cameras were placed outside the main vacuum chamber, in separate vacuum chambers equipped with 50 μm thick *kapton* (x-ray transparent) windows. An additional Be filter was used to shield CCDs against visible light.

Cylindrical lead collimators with 10 mm thick walls and a clear aperture of about 10 mm diameter were placed between the pin-hole and the x-ray output window of the main chamber to reduce scattered photon noise inside the vacuum chamber. Also, a set of magnets (with typical magnetic field strength of about 1 T) were placed inside each tube in order to stop high energy electrons. All these measures were adopted to reduce as much as possible x-rays produced by electron-impact with the tube walls and the filters. Finally, in order for the two CCD cameras to operate in the single-photon regime, up to 20 mylar foils (each one 50 μm thick) were used for each pin-hole camera to reduce the flux to the required level.

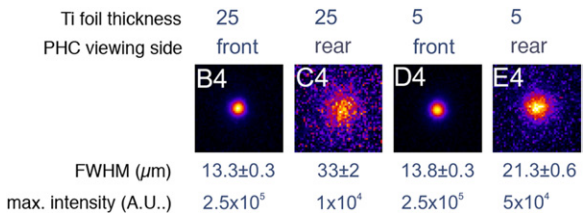

Figure 3. Front and rear side images of the x-ray source obtained at a laser intensity of 5×10^{19} W cm^{-2} for two different target thicknesses of 5 and 25 μm. The dimension of the images is 120 μm $\times$ 120 μm. Images were obtained adding up about 110 images obtained in the identical experimental conditions. In each image, the intensity is rescaled to use the entire colour range. The FWHMs are also reported as measured after background subtraction from the lineouts of the source taken along vertical diameters.

Given the pin-hole camera magnification (10$\times$) and considering the pixel size of the two CCDs ($26 \times 26\,\mu$m^2), the spatial resolution achievable by the pin-hole cameras was mainly limited by the pin-hole diameter and is therefore expected to be approximately 5 μm. More quantitative information on the performances of our imaging system in terms of spatial resolution was obtained by using Ti foils and by running the pin-hole cameras in the standard high flux condition (no energy resolution). A summary of these results is given in the following section.

4. X-ray imaging of interactions with Ti foil targets

In figure 3 we show a comparison of front and rear side images of the x-ray source obtained at a laser intensity of 5×10^{19} W cm^{-2} for two different target thicknesses of 5 and 25 μm. The size of the imaged area is 120 μm $\times$ 120 μm. The 45° observation angle was not accounted for to show full details of the uncorrected image. We point out here that in the general case of extended, 3D emission region (e.g. propagation in thick, layered target as described below), correction of the observation angle falls in the general tomography-like reconstruction procedure and is therefore not straightforward. Even if for 5 μm target foils this would be an immediate task, for 25 μm thick target foils this would be not straightforward. In the 5 μm thick foil case the size of the source is comparable with the target thickness and it is impossible to say where photons are coming from. In this case no filters were used, i.e. the images are not energy resolved. The images were obtained by adding up about 100 single images. To avoid instrumental source broadening due to residual source displacement from shot to shot, the center of mass of a 50 $\times$ 50 pixel square around the source was calculated. Possible shifts were compensated and then the images were added up as discussed in [16].

The FWHM source size reported for each image was measured along a vertical diameter to avoid the effect of differential attenuation of the x-ray signal expected in the horizontal direction due to the angle between the observation axis and the target plane. Also shown in the image are the relative maximum x-ray intensity for the four images. Accordingly, a strong attenuation of the signal in the rear side image is found with respect to the front side emission. This attenuation can be possibly explained as due to the absorption of the x-ray radiation in the target substrate. However, since the attenuation length for Ti Kα photons in Ti is 20.3 μm, a quantitative explanation of the observed attenuation requires additional information. We also observe that the rear side images show a source size that is significantly larger than the size measured from the front side images (2.5 times in the case of the 25 μm thick target and 1.5 times in the case of the 5 μm thick target). These observations suggest a possible role of

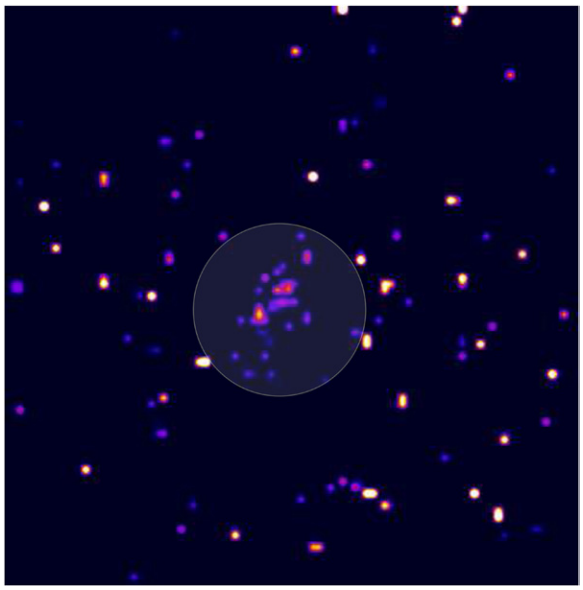

Figure 4. Typical raw data showing the low flux image obtained from the detection of individual x-ray photons by a CCD detector coupled to a pin-hole camera. The 50 μm diameter circular area at the centre of the image identifies the region where the image of the source is located. The events outside this region are due to diffuse scattering and are discarded during the analysis. Such an image is obtained from one laser shot. As in the case of figure 1, each photon generates a charge proportional to its energy. In addition, in this case the position of each event of the CCD detector is also measured to reconstruct the full image at any given photon energy.

non-isotropic radiation emission mechanisms that give different contribution to the front and the rear side pin-hole cameras. A possible role of directional bremsstrahlung (see [8, 19]) is under investigation and additional experimental evidence is given below.

5. Application to the imaging of multilayer targets

Multilayer targets are usually employed in order to use x-ray emission at different depths inside the target by the 'tracer layers' as a marker of fast electron propagation. It is well known that layer transition in this kind of targets is expected to generate some perturbation in the fast electron propagation, due to the discontinuity of important parameters like material density, conductivity, etc. Nevertheless, important information on the energy deposition can still be obtained as demonstrated in recent studies (see [20] and references therein). In these studies, single energy x-ray imaging with micrometre scale spatial resolution was indeed exploited to infer substrate heating due to fast electron energy deposition.

Here, we briefly show how our novel imaging technique can be used to perform multi-energy x-ray imaging with a comparable spatial resolution. To this purpose we will show some results obtained from laser irradiation of a target consisting of three metallic layers obtained from galvanic deposition of Cr and Ni on a Fe substrate. The first layer (laser side) was 1.2 μm thick Cr, the middle layer was a 10.9 μm thick Ni and a third layer (on the rear side) was a 10 μm thick Fe.

Energy resolving imaging was applied setting the CCD detector work in the low flux regime. A typical raw data x-ray image shown in figure 4 consists of a small number of events

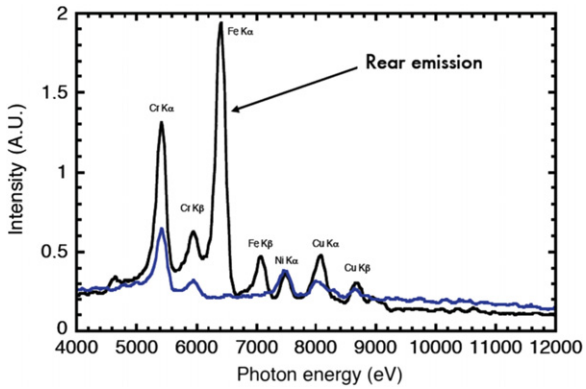

Figure 5. X-ray spectrum of the x-ray radiation detected from the front and the rear of a three-layer Cr–Ni–Fe target target irradiated at an intensity of 5×10^{19} W cm^{-2}. The spectrum was obtained adding up all identified photon from the analysis of the low flux images obtained from 350 laser shots. The target was irradiated on the Cr side. Note that the relative intensities of the two spectra are not in scale.

Table 1. $K\alpha$ and $K\beta$ line emission energy for the elements used in our multilayer target.

Element	Kα (keV)	Kβ (keV)
Cr	5.41	5.95
Ni	7.48	8.26
Fe	6.40	7.06

(each with its own shape and signal amplitude) corresponding to a single-photon interactions with the CCD detector.

Each CCD acquisition (corresponding to one laser shot) is then analysed in order to retrieve the total charge released and the landing position of each x-ray photon on the CCD sensitive surface. As described above, a dedicated reconstruction algorithm is then used to measure the charge of each photon. As a result, the total spectrum of the x-ray emission from the target can be obtained, after adding up the contribution from a few hundreds of laser shots (i.e. CCD acquisitions).

Figure 5 shows the spectrum obtained by our front and rear side diagnostics (integrated over 350 shots). Table 1 reports the energies of the Kα and Kβ emission lines from the target materials. From the width of the lines we find that the spectral resolution is about 90 eV. This value of the resolution is mainly due to the width of the ADC level distribution of the intrinsic background noise of the CCD. This is a characteristic figure of the CCD that makes the charge produced by monochromatic x-ray photons at a given energy spread over a finite width. The main Kα and Kβ line emissions from the Cr layer are clearly visible on the front and rear side images. The Ni Kα emission is also clearly visible from both sides of the target, while Fe Kα and Kβ are clearly visible only from the rear side. Cu emission visible in both spectra is likely to arise from impurities in the Fe and Ni substrates. We observe here that the difference in the line intensity between the front and rear side spectra are also due to the filters and to the photon propagation and attenuation through the different layers. Therefore a quantitative analysis of these relative intensities will have to take into account this effect also.

Finally, energy resolved images of the source at any given energy can be obtained by selecting the corresponding photons from the spectral distribution, by plotting them according

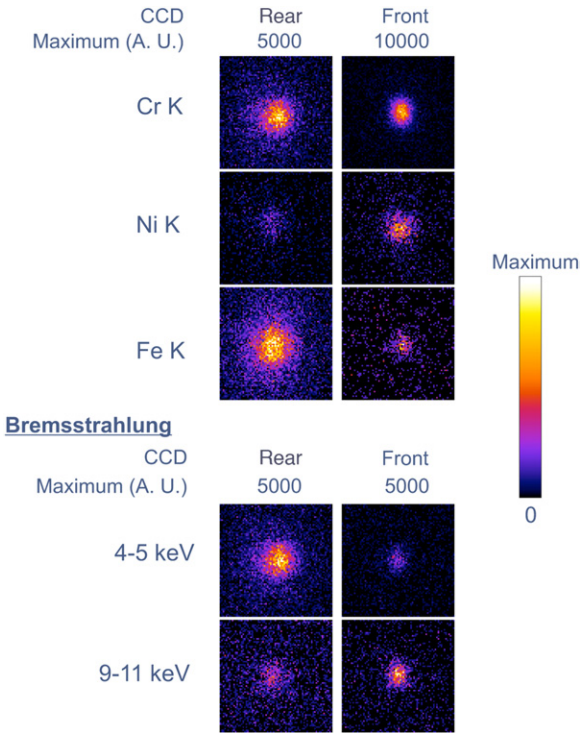

Figure 6. Energy resolved images of the Kα sources of Cr, Ni and Fe as seen from the rear (left) and the front of the target obtained selecting all the photons within a spectral window of ± 230 eV. The lower part of the figure shows the images of the source obtained selecting the photons in two regions where no or weak line emission is expected to occur and where the main contribution is expected to be given by bremsstrahlung emissions. The images were not corrected for the absorption of the Kα radiation, through target layers, filters, etc. The maximum of the colour scale is reported in each case. The dimension of each image is $180 \times 180\sqrt{2}\,\mu\text{m}^2$.

to their position on the CCD detector and by taking into account the geometry of the pin-hole camera imaging system, including the magnification. Figure 6 shows the energy resolved full imaging of the x-ray source at the Kα and Kβ line energy of the three materials, as seen by the front and rear side pin-hole cameras. In this case, a total of 1600 single shot images were used.

The upper side of figure 6 shows the images obtained selecting x-ray photons in an energy window around each Kα line (± 230 eV). In the lower side of the figure we report the images obtained selecting x-ray photons in a spectral region where no spectral lines are expected, i.e. below the Cr–Kα and above the Ni–Kα. Therefore, contribution to these images will mainly come from continuum radiation, possibly arising from bremsstrahlung emission. Higher energies photons are also present in the spectrum, however, for these energetic photons the 2.5 μm thick, pin-hole Pt substrate will start becoming transparent and the contrast of the pin-hole image will consequently decrease.

In general, a careful analysis of the spectrally resolved images of figure 6 can be used to identify all contributions from each layer of the target and to reconstruct the propagation of the fast electron beam through the whole target. In fact, by measuring the exact position and size of each emission component one can reconstruct all possible sources of emission. Thanks to our novel imaging technique, the photon energy and spatial data as briefly described above provide sufficient information to enable an evaluation of the contribution of each layer

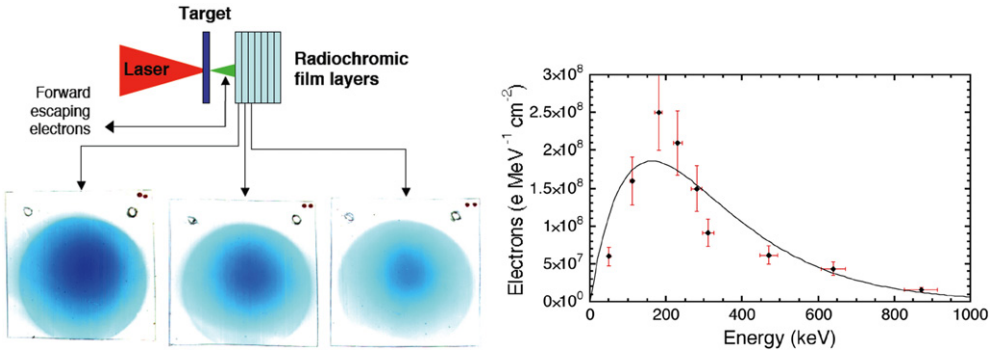

Figure 7. (Left) Scan of the first three radiochromic film layers placed behind the target, along the laser propagation direction showing the raw cross-section image of the forward escaping fast electrons generated in the same condition as the ones in figure 6. (Right) Spectrum of the electrons retrieved using all radiochromic film layers according to [21]. Also shown in the plot for comparison is the curve corresponding to the relativistic Maxwellian distribution at 160 keV.

of the target to the x-ray emission. Such a characterization, which is currently in progress, will provide the information needed for a detailed comparison of emission properties as measured experimentally with the corresponding quantities as calculated by a numerical code capable of describing transport and energy deposition of fast electrons in matter and consequent emission of characteristic x-ray radiation.

Additional information concerning the fast electron distribution was obtained from the experiment by direct measurement of forward escaping electrons (figure 7). These measurements, performed using a calibrated stack of radiochromic films [21] show a fast electron distribution that is consistent with a relativistic Maxwellian distribution with a characteristic temperature of 160 keV.

Modelling of our results on Kα imaging is being carried out using the code PETRA [22] to calculate expected x-ray fluorescence from the target assuming a given fast electron distribution. PETRA is a 3D hybrid code for transport of relativistic electrons in dense plasma: fast electrons are coupled to low temperature electron background fluid by collective fields (PIC procedure) and collisions (Monte Carlo procedure). Fast electrons are injected in the target as a beam with a Maxwellian relativistic distribution and local temperature taken from [23] at different regions of the focal spot. The distribution in space and time for the injected fast electron beam is Gaussian. The target substrate is described by its specific heat as an interpolation of the Fermi-Dirac electronic specific heat and the ideal gas specific heat and by its resistivity based upon a modified [24] Spitzer model. Finally, Kα emission is calculated from the impact ionization cross-section. A preliminary simulation was carried out using a single layer target consisting if a 30 μm thick Fe. The plot in figure 8 shows the fast electron beam density after propagation in a 30 μm thick Fe layer calculated using the hybrid code PETRA.

The initial fast electron beam energy distribution is assumed to have a relativistic Mawellian distribution whose temperature is obtained from the measurements of figure 7 (right) after the Bethe–Bloch calculation to retrieve the electron distribution before propagation in the target. The pulse duration is 100 fs and the diameter of the fast electron beam at the target surface is assumed to be 2.6 μm to match the focal spot size of our experimental setup. According to this plot, the fast electron beam undergoes a significant diffusion in the target that makes the beam size increase by a factor of two or more at the exit of the target. In fact, Kα emission calculated by the code during this fast electron propagation has a source size

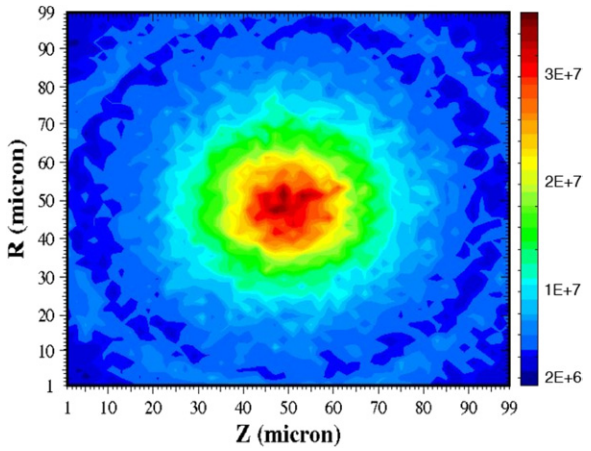

Figure 8. Fast electron beam density after propagation in a 30 μm thick Fe layer calculated using the hybrid code PETRA. The initial fast electron beam diameter at the target surface is 2.6 μm and the pulse duration is 100 fs.

with a main component of approximately 10 μm FWHM, while lower intensity tails of the emission extend up to a 50 μm from the axis. These calculation are now under extensive test and quantitative comparison with the measurements described above.

6. Summary and conclusions

In summary, we reported on the first results of a novel experimental technique for the full imaging with spectral resolution of the x-ray emission from laser irradiated targets. This technique, based upon a pin-hole camera equipped with a CCD detector operating in the so-called single-photon regime, allows the image in any given spectral window in the keV range to be obtained, provided that the x-ray response of the CCD has been previously characterized. Furthermore, the absolute photon flux in each selected energy range can be retrieved, once the collection efficiency of the setup and the detector quantum efficiency are considered.

We have shown a first use of the technique for studying the propagation of fast electrons inside the target by using multilayer targets, whose fluorescence emission from each layer due to fast electron propagation was successfully imaged with a spatial resolution of about 5 μm and a spectral resolution of about 90 eV.

The technique 'as it is' has currently a 'multi-shot' basis due to the need for a statistically significant number of photons to be detected. The number of shots could be reduced by using a higher magnification, which would enable to collect a greater number of photons per shot, while satisfying the single-photon condition on the CCD detector. Another possibility is to exploit large area CCDs or similar position sensitive devices in combination with a pin-hole array, to collect more than one 'single-photon image' on the same CCD detector.

Acknowledgments

This work was funded by the MIUR SPARX and MIUR-FSRIS project 'Impianti Innovativi multiscopo per la produzione di radiazione X' and by the INFN project PLASMON-X and by the Deutsche Forschungsgemeinschaft. Access to the IOQ installation was supported by LASERLAB. We also thank F Cornolti from the Physics Department of the University of Pisa

for fruitful discussions and suggestions on the preliminary modeling of the data. One of us (AA) acknowledges financial support by the 'Programma Ingenio'.

References

[1] Tabak M, Hammer J, Glinsky M E, Kruer W L, Wilks S C, Woodworth J, Campbell E M, Perry M D and Mason R J 1994 *Phys. Plasmas* **1** 1626–34
[2] HiPER *Technical Design Report* http://www.hiper-laser.org
[3] Nishimura H *et al* 2003 *J. Quantum Spectrosc. Radiat. Transfer* **81** 327
[4] Freeman R *et al* 2003 *J. Quantum Spectrosc. Radiat. Transfer* **81** 183
[5] Batani D *et al* 2002 *Phys. Rev.* E **65** 066409
[6] Yasuike K, Key M H, Hatchett S P, Snavely R A and Wharton K B 2001 *Rev. Sci. Instrum.* **72** 1236–40
[7] Norreys P A *et al* 1999 *Phys. Plasmas* **6** 2150
[8] Sentoku Y, Mima K, Taguchi T, Miyamoto S and Kishimoto Y 1998 *Phys. Plasmas* **5** 4366–72
[9] King J A *et al* 2005 *Rev. Sci. Instrum.* **76** 076102
[10] Stoeckl C, Theobald W, Sangster T C, Key M H, Patel P, Zhang B B, Clarke R, Karsch S and Norreys P 2004 *Rev. Sci. Instrum.* **75** 3705–7
[11] Gizzi L A, Giulietti A, Giulietti D, Audebert P, Bastiani S, Geindre J-P and Mysyrowicz A 1996 *Phys. Rev. Lett.* **76** 2278–81
[12] Labate L, Galimberti M, Giulietti A, Giulietti D, Köster P, Tomassini P and Gizzi L A 2007 *Appl. Phys.* B **86** 229–33
[13] Park H S, Izumi N, Key M H, Koch J A, Landen O L, Patel P K, Phillips T W and Zhang B B 2004 *Rev. Sci. Instrum.* **75** 4048–50
[14] Gruner S M, Tate M W and Eikenberry E F 2002 *Rev. Sci. Instrum.* **73** 2815–42
[15] Howe J, Chambers D M, Courtois C, Förster E, Gregory C D, Hall I M, Renner O, Uschmann I and Woolsey N C 2006 *Rev. Sci. Instrum.* **77** 036105
[16] Labate L, Giulietti A, Giulietti D, Köster P and Gizzi L A 2007 *Rev. Sci. Instrum.* at press
[17] Fraser G W 1989 *X-ray Detectors in Astronomy* (Cambridge: Cambridge University Press)
[18] Labate L, Galimberti M, Giulietti A, Giulietti D, Gizzi L A, Tomassini P and Di Cocco G 2002 *Nucl. Instrum. Methods* A **495** 148–53
[19] Sheng Z M, Sentoku Y, Mima K, Zhang J, Yu W and Meyer-ter-Vehn J 2002 *Phys. Rev. Lett.* **85** 5340
[20] Batani D 2002 *Laser Part. Beams* **20** 321–36
[21] Galimberti M, Giulietti A, Giulietti D and Gizzi L A 2005 SHEEBA: a spatial high energy electron beam analyzer *Rev. Sci. Instrum.* **76** 053303
[22] Honrubia X *et al* 2004 *Laser Part. Beams* **22** 129–35
[23] Beg F *et al* 1997 *Phys. Plasmas* **4** 447–57
[24] Benuzzi A *et al* 1998 *Phys. Plasma* **5** 2410